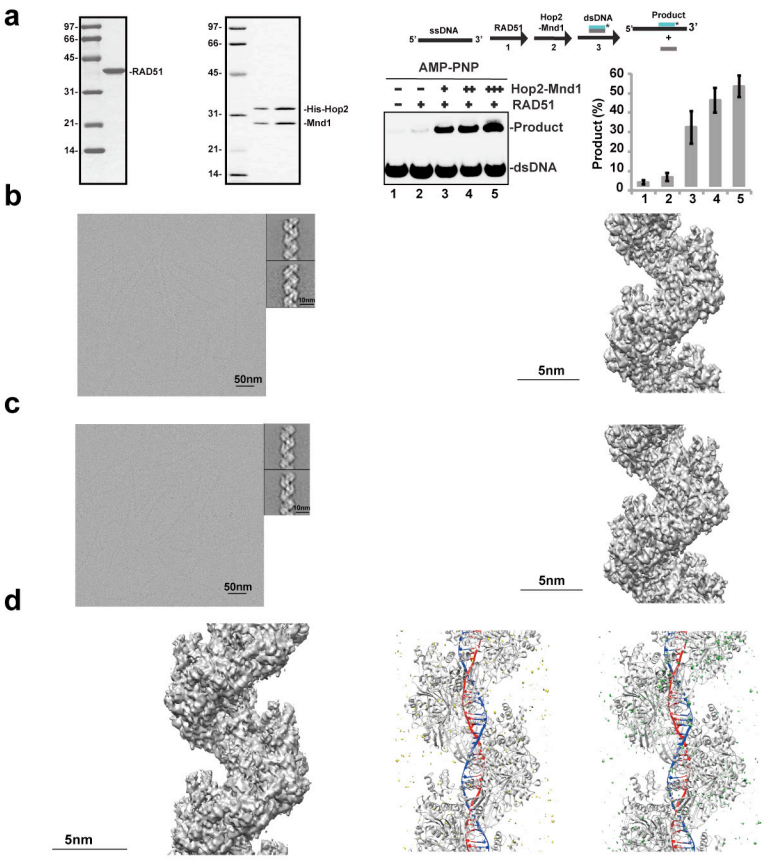

Supplementary Figure 1

Assembly of RAD51 presynaptic and post-synaptic complex by cryo-EM analysis.

(a) Purified human RAD51 and mouse Hop2-Mnd1 were analyzed by SDS-PAGE with Coomassie blue staining and by DNA strand exchange assays. The reaction scheme setup is illustrated. "+" stands for the concentration of Hop2-Mnd1 and +, ++, +++ means 100 nM, 200 nM, and 400 nM, respectively. Rad51 concentration was kept constant at 2 mM in all the assays. The mean values ± s.d. from three independent experiments were presented as bar diagram on the right panel. (b) A representative cryo-EM micrograph of presynaptic filaments and a representative 2D class average are shown in the left panel. 3D reconstruction of the presynaptic filament via IHRSR is shown on the right. (c) A representative cryo-EM micrograph of post-synaptic filaments and a representative 2D class average are shown in the left panel. 3D reconstruction of the post-synaptic complex is shown on the right. (d) 3D reconstruction of the RAD51-ssDNA presynaptic complex incubated with Hop2-Mnd1 is shown on the left panel. The difference map between 3D reconstructions of RAD51-ssDNA presynaptic complex with and without Hop2-Mnd1 incubation is shown in the middle and the right panels with inverted contrast separately.

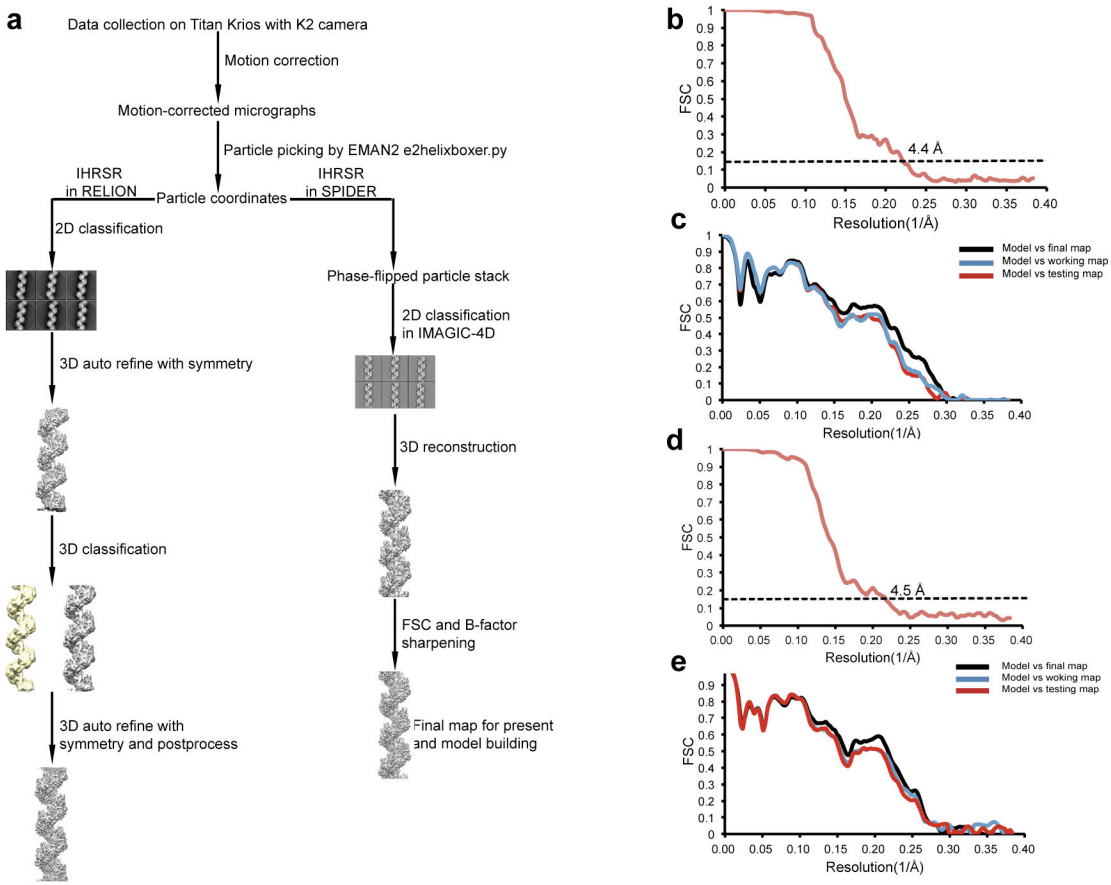

Supplementary Figure 2

Structure determination of presynaptic and post-synaptic complexes.

(a) Work flow for 3D reconstruction of the presynaptic and post-synaptic complexes using two alternative strategies. (b) and (d) show respectively the Fourier shell correlation (FSC) curves of the presynaptic and post-synaptic complexes between maps calculated from two independent half datasets. (c) and (e) show respectively the FSC curves of the presynaptic and post-synaptic complexes between the built atomic models and the 3D density maps (black, final refined atomic model versus final map; blue, final refined model versus working map; red, final model versus testing map).

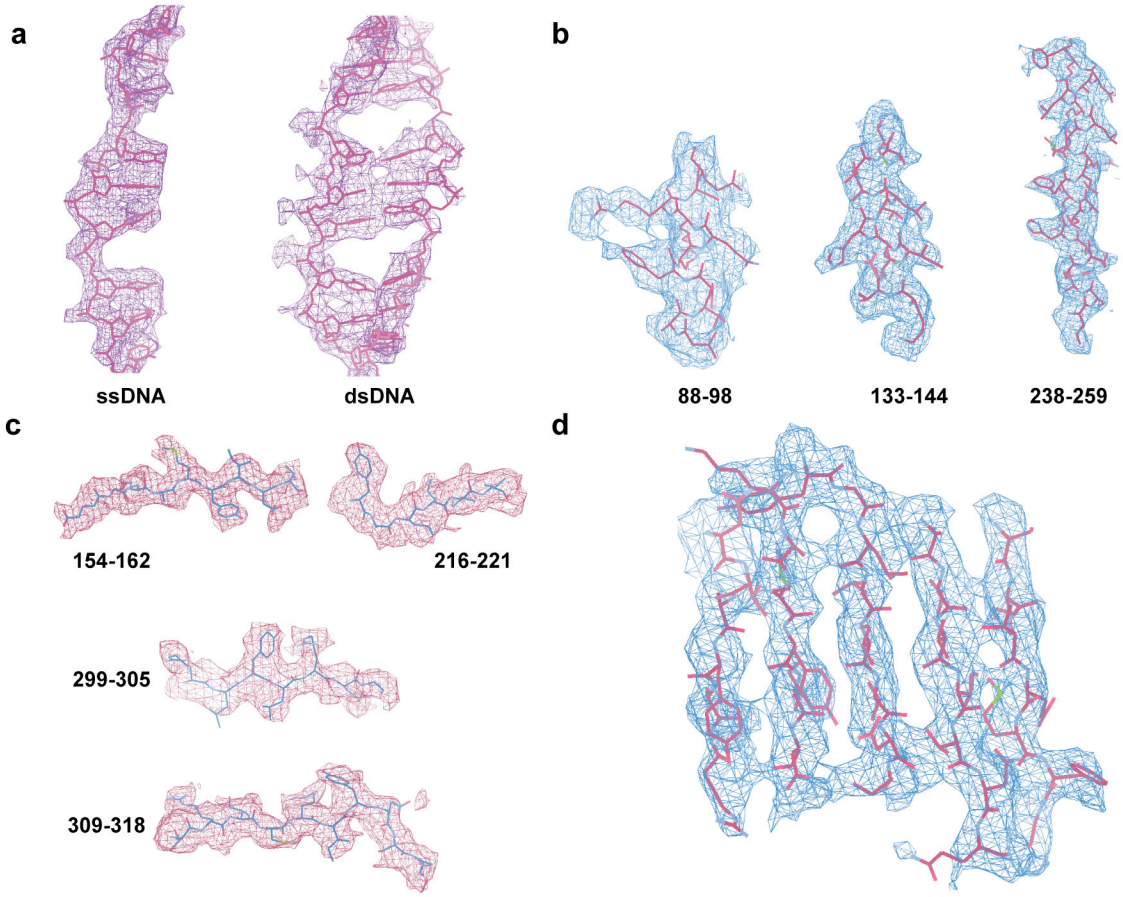

Supplementary Figure 3

Representative EM densities with the corresponding atomic models.

(a) The ssDNA and dsDNA selected from presynaptic complex and post-synaptic complex, respectively. (b) Selected three α-helix elements. (c) Selected 4 β-strand elements. (d) The β-sheet motif in the middle of RAD51's ATPase core.

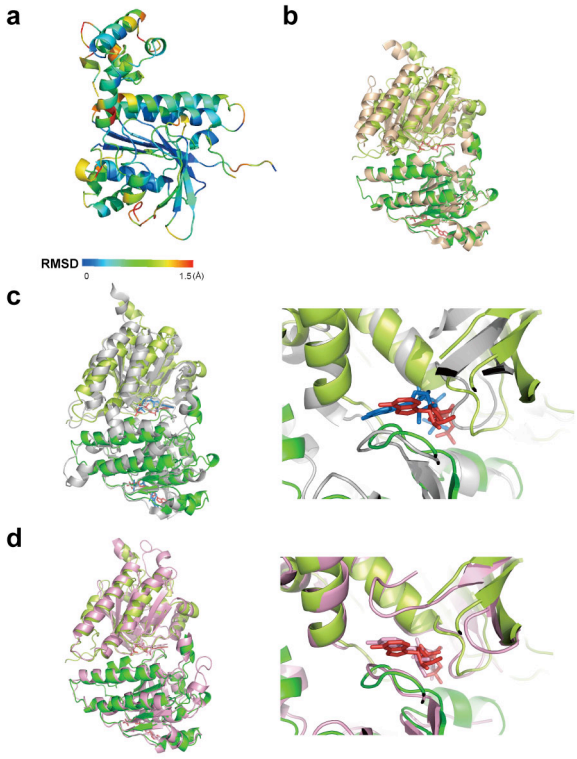

Supplementary Figure 4

Structural comparison of RAD51 and orthologs in their nucleotide binding sites at the protomer interface.

(a) RAD51 protomers from the presynaptic and post-synaptic complexes are superimposed, colored by the RMSD value between the two atomic models. (b) The presynaptic filaments of human RAD51 (green and light green for two protomers) and yeast Rad51 filament (salmon) are superimposed with the models of lower protomers aligned to each other. (c) The superimposition of presynaptic filaments of human RAD51 (green and light green for two protomers) and *E.coli* RecA (grey) with the models of lower protomers aligned to each other. An enlarged view of the nucleotide binding pocket is shown on the right. (d) The superimposition of human RAD51 and *Methanococus Voltae* RadA (pink) with the models of the lower protomers aligned to each other. An enlarged view of the nucleotide binding pocket is shown on the right.

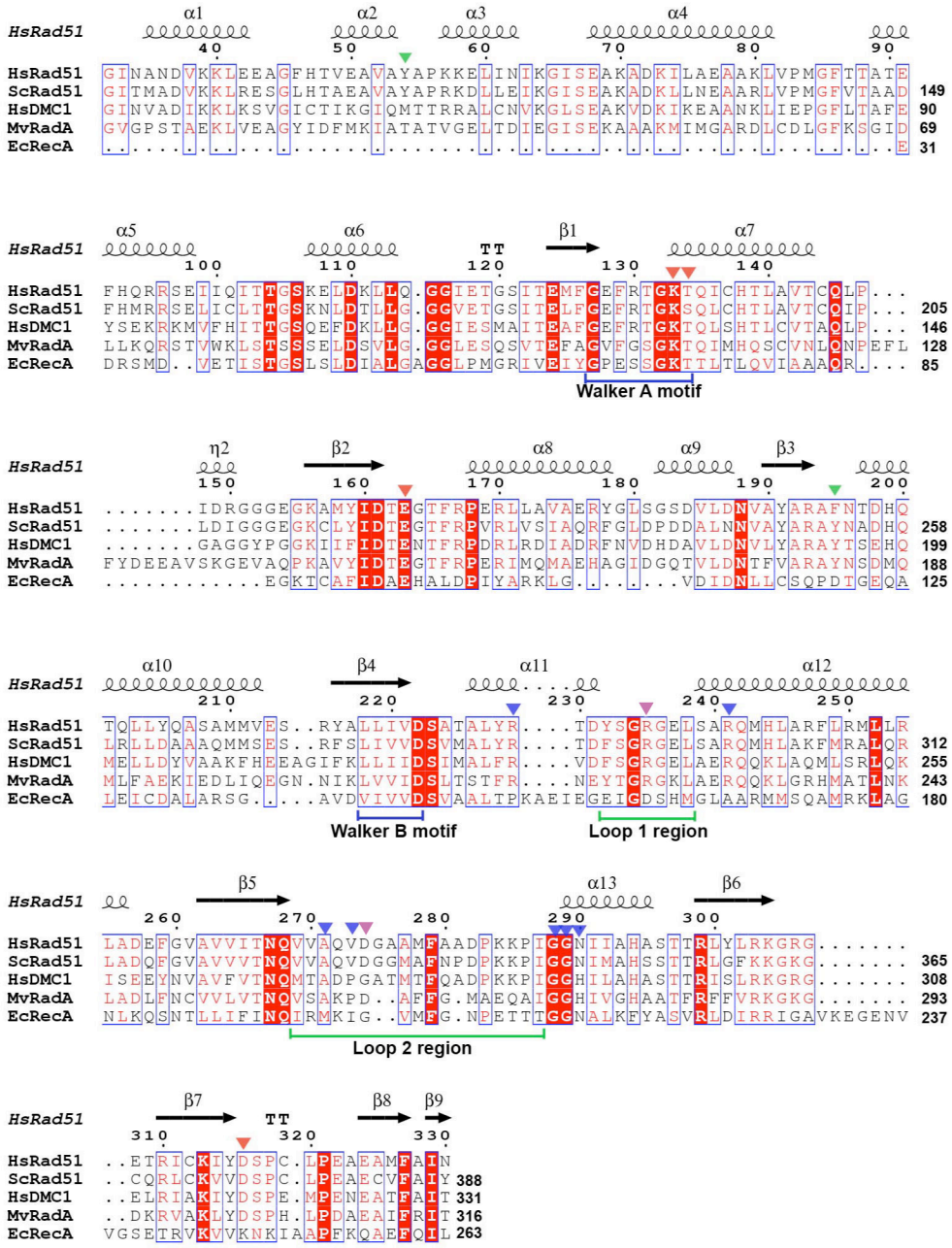

Supplementary Figure 5

Sequence alignment of Human RAD51 and its orthologs.

The secondary structural elements of human RAD51 determined in our structure are labeled on top of the corresponding residues. Walker A and B motifs involved in nucleotide binding, the conserved Loop 1 and Loop 2 regions responsible for binding ssDNA or dsDNA, and key residues for human RAD51 function are all labeled. Y54 and F195 that are located in the interface of human RAD51 protomers are shown in green triangles. K133, T134, E163, and D316 that interact with AMP-PNP-Mg^{2+} are shown in red triangles. The blue triangles of R229, R241, A271, V273, G288, G289, and N290 are involved in ssDNA binding, also shown in Figure 2. R235 and D274 in magenta triangles involved in dsDNA binding are also shown in Figure 2.

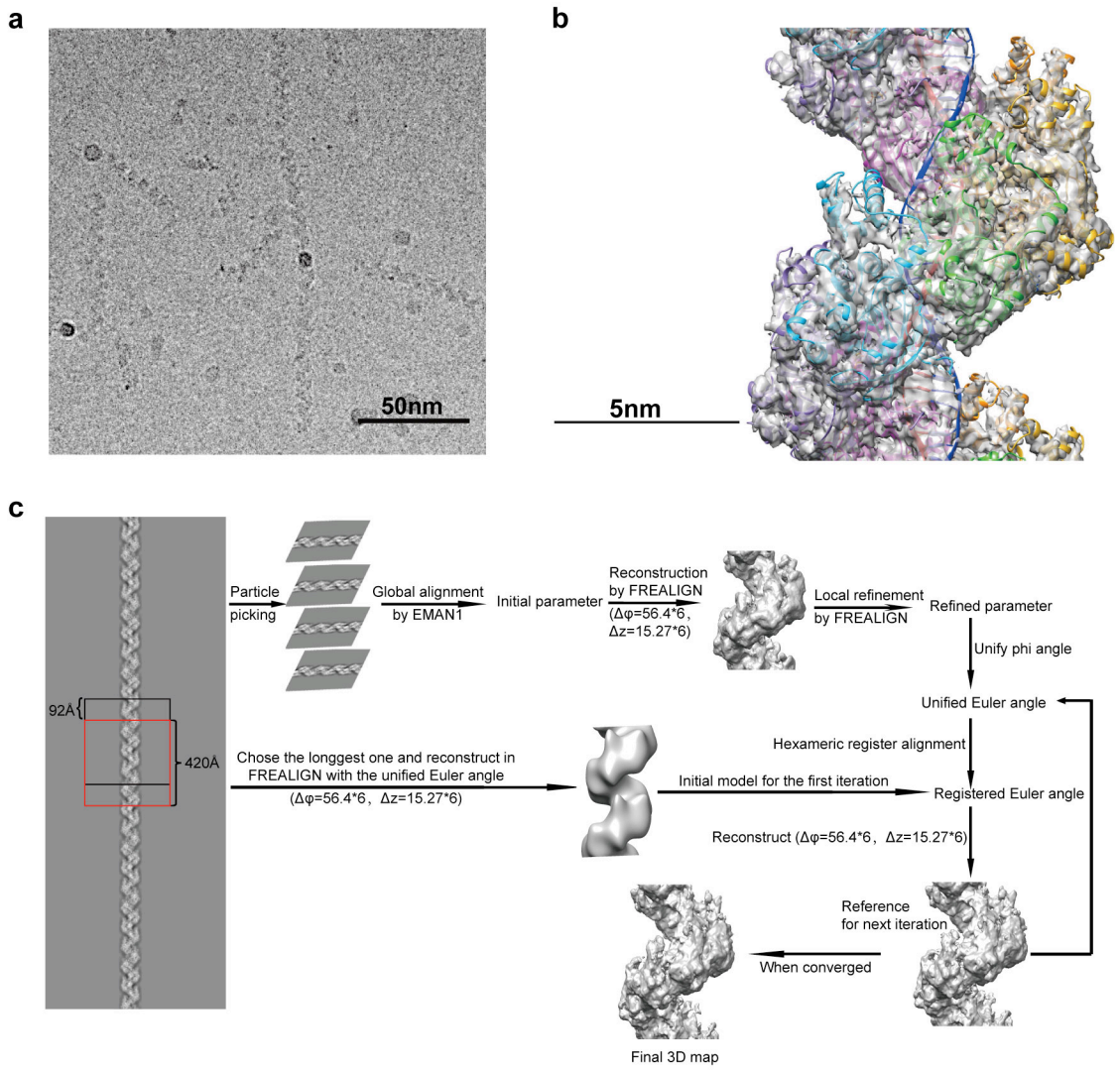

Supplementary Figure 6

Cryo-EM of the arrested state of RAD51-mediated strand exchange and work flow of the algorithm to reconstruct the arrested synaptic complex with hexameric repeat helical symmetry.

(a) A representative cryo-EM micrograph of the arrested synaptic complex. (b) Semitransparent rendering of the 3D reconstruction of the arrested synaptic complex via IHRSR using the helical parameters of RAD51 monomer as asymmetric unit. The post-synaptic complex atomic model is docked in the density for comparison. (c) Particles were segmented from filaments with non-overlap of about 92 Å, corresponding to a hexameric rise. During refinement the spatial relationship between neighboring particles from the same filament was taken into account, as was the relationship for different filaments. Details of the algorithm are described in Online Methods.

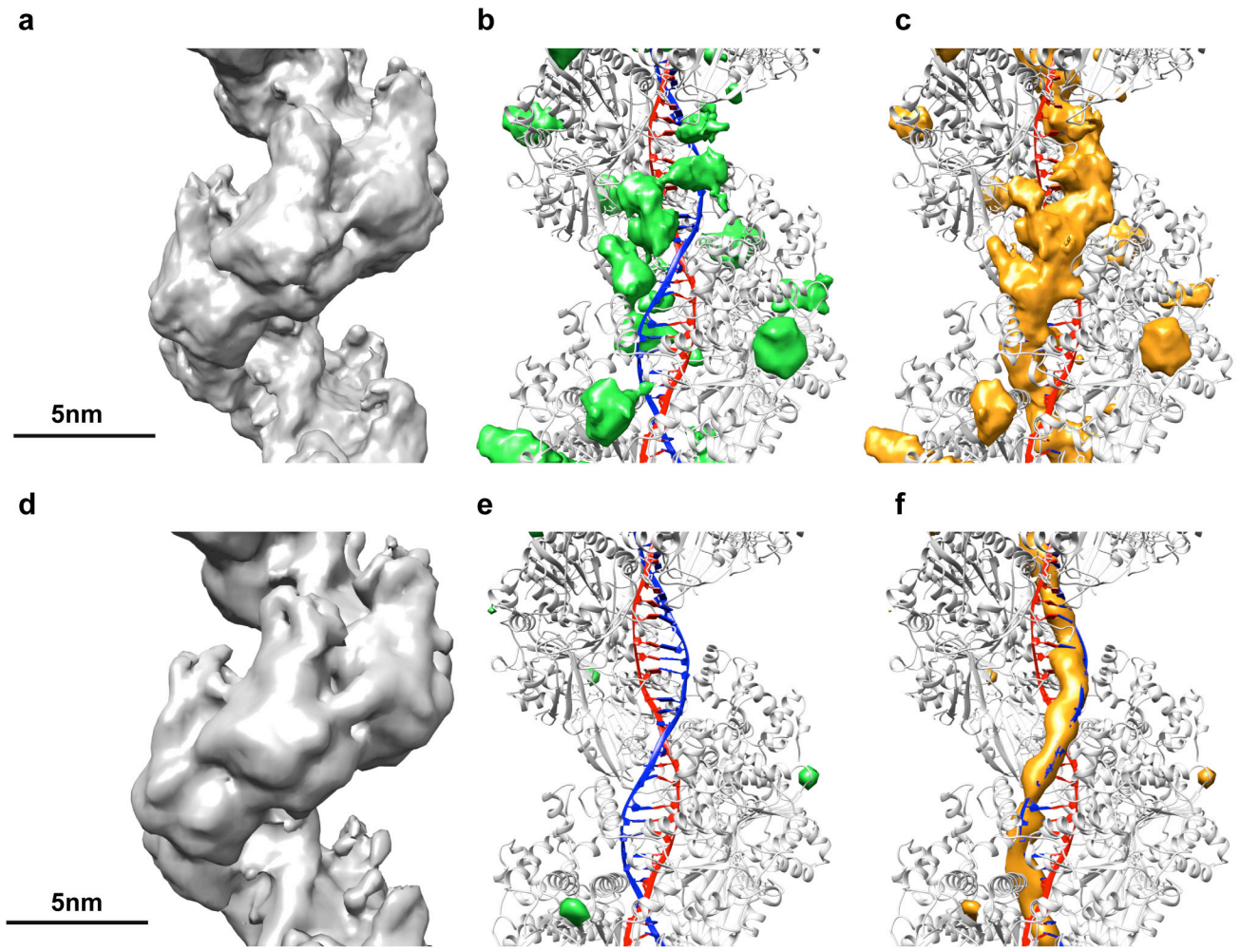

Supplementary Figure 7

Structure analysis of the arrested state of DNA strand exchange.

(a) 3D reconstruction of the arrested synaptic complex via the algorithm described in Figure S7. (b) and (c) show difference maps between the 3D reconstruction and the atomic models of the post-synaptic complex and presynaptic complex, respectively. (d) 3D reconstruction of the post-synaptic complex dataset using the same algorithm as for the arrested synaptic complex. (e) and (f) are difference maps between the 3D reconstruction and the atomic models of the post-synaptic and presynaptic complexes, respectively. Please be noted that the extra densities on the outer surface of RAD51's N-terminal domains are due to the lack of the very N-terminal 21 residues in the atomic models. These extra densities are hidden in Figure 4b in order to show the extra densities near the nucleic acids more clearly. All the difference maps in (b), (c), (e), (f) are shown in a threshold of 8σ.